

## Research Article

# The Mechanical Alloying Behavior of Fe<sub>2</sub>O<sub>3</sub> into NiO in the High-Energy Ball-Milling Process

Y. Z. Zhu <sup>1</sup>, Y. Liu,<sup>1</sup> H. Huang,<sup>2</sup> Y. Y. Guo,<sup>1</sup> S. Y. Yin,<sup>1</sup> and F. W. Hu<sup>1</sup>

<sup>1</sup>Provincial Key Lab of Hard Materials, North China University of Technology, Beijing 100144, China

<sup>2</sup>College of Architecture and Civil Engineering, Beijing University of Technology, Beijing 100124, China

Correspondence should be addressed to Y. Z. Zhu; tozyz1@163.com

Received 27 January 2021; Revised 9 March 2021; Accepted 4 May 2021; Published 18 May 2021

Academic Editor: Patrice Berthod

Copyright © 2021 Y. Z. Zhu et al. This is an open access article distributed under the Creative Commons Attribution License, which permits unrestricted use, distribution, and reproduction in any medium, provided the original work is properly cited.

The NiO and Fe<sub>2</sub>O<sub>3</sub> powders were mixed by the high-energy ball-milling, followed by a sintering of the mixture at 1340°C for 0.5 h. XRD, SEM, DSC, and size measurements were preformed to study the microstructure evolution in the high-energy ball-milled mixture and the sintered ones, as well. It showed that the high-energy ball-milling processes resulted in a severe lattice distortion in the powder of Fe<sub>2</sub>O<sub>3</sub>, but only a slight lattice distortion in NiO. Meanwhile, a solid solution of iron atoms into the NiO lattice was also detected in the milling process. It was also found that the solubility of the iron atoms into the NiO lattice delayed the synthesizing reaction in the following sintering process.

## 1. Introduction

Most of the oxides are stable at the room temperature [1–4]. NiO and Fe<sub>2</sub>O<sub>3</sub> are the typical ones of these oxides. They are often used as raw materials to synthesize ceramics, for instance, NiFe<sub>2</sub>O<sub>4</sub>. However, the transformation efficiency of both oxides into the ceramics is often limited by their stable microstructures in a usual sintering process [5]. Thus, it is necessary to understand the possible parameters in both the mixing and the sintering processes of the powders, which affects their synthesizing reaction in the sintering process.

High-energy ball-milling is a process that mixes multiple raw powders with greater efficiency before their sintering process [6, 7]. It may alter the microstructure of the powder mixture. In the high-energy ball-milling process, powder particles are possibly broken and undergo significant plastic deformation [8–12]. Thus, a subsequent reaction may be changed in the milled powder mixture in the following sintering processes [13–15].

Researches are available on synthesizing of NiFe<sub>2</sub>O<sub>4</sub> ceramics by sintering of the NiO and Fe<sub>2</sub>O<sub>3</sub> powders [16, 17]. But few studies have been reported about the effects of high-energy ball-milling on the microstructure of these two powders, especially its effect on the subsequent synthesizing

reaction. The main aim of this study is to clarify the microstructure evolution of the NiO and Fe<sub>2</sub>O<sub>3</sub> powders and the possible interaction behavior between them in the high-energy ball-milling process, and further to evaluate its effect on the following sintering reaction.

## 2. Experimental Works

The purity of the as-received powders of NiO and Fe<sub>2</sub>O<sub>3</sub> was no less than 99.0%. The mean sizes of both powder particles were 1.4 μm and 10 μm, respectively.

Both powders were ball-milled in an ND7 planetary mill for 0.5, 2, 5, and, 10 h, respectively. The ball to powder weight ratio was 7 : 1. The molar proportion of Fe<sub>2</sub>O<sub>3</sub>/NiO powders was 11:10 to ensure a complete surface contact between the NiO and Fe<sub>2</sub>O<sub>3</sub> powders because the size of the Fe<sub>2</sub>O<sub>3</sub> particle was much larger than that of NiO.

The whole high-energy ball-milling mixing process parameters are illustrated in Table 1.

All of the milled powders were dispersed in a solution with 99.99 wt.% alcohol using an ultrasonic system and then dried for further microstructure measurements and sintering experiment. In this sintering process, no cold densifying was performed, and only the effect of the sintering

TABLE 1: The parameters of the ball milling process.

Frequency (Hz)	Current (A)	Rotation speed (r/min)	Output voltage (V)	Number of the steel balls	Weight of charge ratio	Condition
24.5	0.9	244	334	φ20:φ10:φ6 = 10:104:170	2:1	Drying milling

temperatures on the microstructure transformation was considered. Thus, part of the milled powders was sintered at 1340°C for 0.5 h. Both the microstructures of the milled powders and the sintered ones were measured in the study.

Size measurement of the milled powders was performed using the MASTERSIZER 2000 size analysis system. The micrograph of the powders was observed on a Navo 400 field emission SEM system at a voltage of 20 kV. X-Ray powder diffraction analysis was carried out using a SHIMADZU XRD-6000 X-ray powder diffractometer. Cu-K $\alpha$  radiation and a scanning speed of 0.03342°/min were utilized. Phases were identified using the Bruker EVA (evaluation) software. Quantitative phase, grain size, and microresidual stress analyses were implemented using the software Topas3. Thermogravimetric analysis was performed on a NETZSCH STA 449C simultaneous TG–DSC–STA system at a heating rate of 10°C/min in the air.

### 3. Results

It is shown in Figure 1 the measured particle size of the powders milled for different hours. Two strong peaks can be observed on the size distribution plot of the powders without subsequent high-energy ball-milling (Figure 1(a)). The first peak occurs at the particle diameter sizing in 1.5  $\mu\text{m}$ , which corresponds to the mean particle size of the as-received Fe<sub>2</sub>O<sub>3</sub> powder. The second peak appears at the particle diameter sizing in approximate 10  $\mu\text{m}$ , which corresponds to the mean particle size of the as-received NiO powder. Around each of these two peaks, the particle sizes of the powders show the Gaussian distribution (Figure 1(a)). However, if the ball-milling time increases from 0 h to 0.5 h, the mean particle size of Fe<sub>2</sub>O<sub>3</sub> shifts from  $\sim 1.5 \mu\text{m}$  to  $\sim 0.6 \mu\text{m}$ , as shown in Figure 1(b), which implies that the Fe<sub>2</sub>O<sub>3</sub> particles were brittle and had been broken in the ball-milling process. NiO particles with an original mean size of  $\sim 10 \mu\text{m}$  remained unchanged with increasing the milling time, which indicates that the NiO particles were hard, ductile, and not easily broken in the ball-milling process. However, the volume fraction of the  $\sim 10 \mu\text{m}$  NiO powder particles (obtained by integration of the whole peak) increased with increasing the ball-milling time (Figures 1(a) and 1(b)). The possible reason for this increase is because the fine hard NiO particles were wrapped with the fine broken Fe<sub>2</sub>O<sub>3</sub> powders in the frequently ball-milling processes, which increased the size of the NiO particle originally finer than 10  $\mu\text{m}$ . Furthermore, a weak peak can be observed at about 3  $\mu\text{m}$  in the plot (Figure 1(b)). This weak peak (also see Figure 1(c)) is possibly owing to the allegation of the Fe<sub>2</sub>O<sub>3</sub> particle or the presence of the minor broken NiO particle.

If the ball-milling time increases to 2 h, the mean size of the small particles shifts from  $\sim 1.5 \mu\text{m}$  of the as-received

powder down to  $\sim 0.3 \mu\text{m}$  of the milled powder, as shown in Figure 1(c). By contrast, no apparent size shift can be observed in the large particles with the mean size of  $\sim 10 \mu\text{m}$  (Figure 1(c)). When the milling time exceeds 2 h, e.g., at 5 and 10 h, the mean size of the large particles remains the same but their relative volume fraction increases with increasing the milling time (comparing Figures 1(d) and 1(e) with Figure 1(a)). The mean size of the small particles increases slightly with increasing the milling time at this time. SEM images of the mixed powders with different milling time are shown in Figure 2. These images demonstrate the size changes of the milled powders.

The X-ray diffraction patterns of the milled powders are shown in Figure 3. It is illustrated that both the intensities and the peak widths of Fe<sub>2</sub>O<sub>3</sub> varied as a function of the milling time. In particular, the intensities decreased and the peak widths were broadened with increasing the milling time. Increases in intensities indicate the accumulation in the volume fraction of Fe<sub>2</sub>O<sub>3</sub> in the mixture. The broadening of the peak widths implies an increase in the microstress and a decrease in the grain size in Fe<sub>2</sub>O<sub>3</sub>. No apparent intensity changes are observed in the diffraction pattern of NiO with increasing the milling time, and very slight broadening may be seen here, as well. Meanwhile, a trace of the Fe<sub>3</sub>O<sub>4</sub> phase was detected in the powders milled for over 2 h, which may be owing to the decreasing in the oxygen partial pressure in the ball mill with increasing the milling time.

Grain sizes determined from the X-ray diffraction patterns are shown in Figure 4. It reveals there is virtually no change in the grain size of the NiO powders with increasing the milling time (see Figure 4(a)). By contrast, the Fe<sub>2</sub>O<sub>3</sub> grain sizes drastically declined from 1  $\mu\text{m}$  before the ball-milling down to 0.2  $\mu\text{m}$  after a ball-milling of 2 hours. The grain size of Fe<sub>2</sub>O<sub>3</sub> further decreased down to 0.01  $\mu\text{m}$  when the ball-milling lasted for 5 hours, and then this grain size became almost constant when the ball-milling time increased from 5 h to 10 h.

For further understanding the dynamical changes that occurred in the high-energy ball-milling process, quantitative calculation of the phases in the powders was performed. The volume fraction of Fe<sub>3</sub>O<sub>4</sub> can be neglected in this calculation because of the low content of this compound in the milled powders detected from the X-ray diffraction. Thus, only NiO and Fe<sub>2</sub>O<sub>3</sub> are considered in the calculation. Furthermore, the effect of the powder texture that resulted from the ball-milling can also be neglected because the milled powders were fully dispersed by ultrasonication. Thus, the diffraction intensities of NiO and Fe<sub>2</sub>O<sub>3</sub> were proportional to their volume fraction in the milled powder mixture. Then, the volume fractions of the milled NiO and Fe<sub>2</sub>O<sub>3</sub> were calculated using the software Topas3, and the relevant results are shown in Figure 5. It is illustrated that the

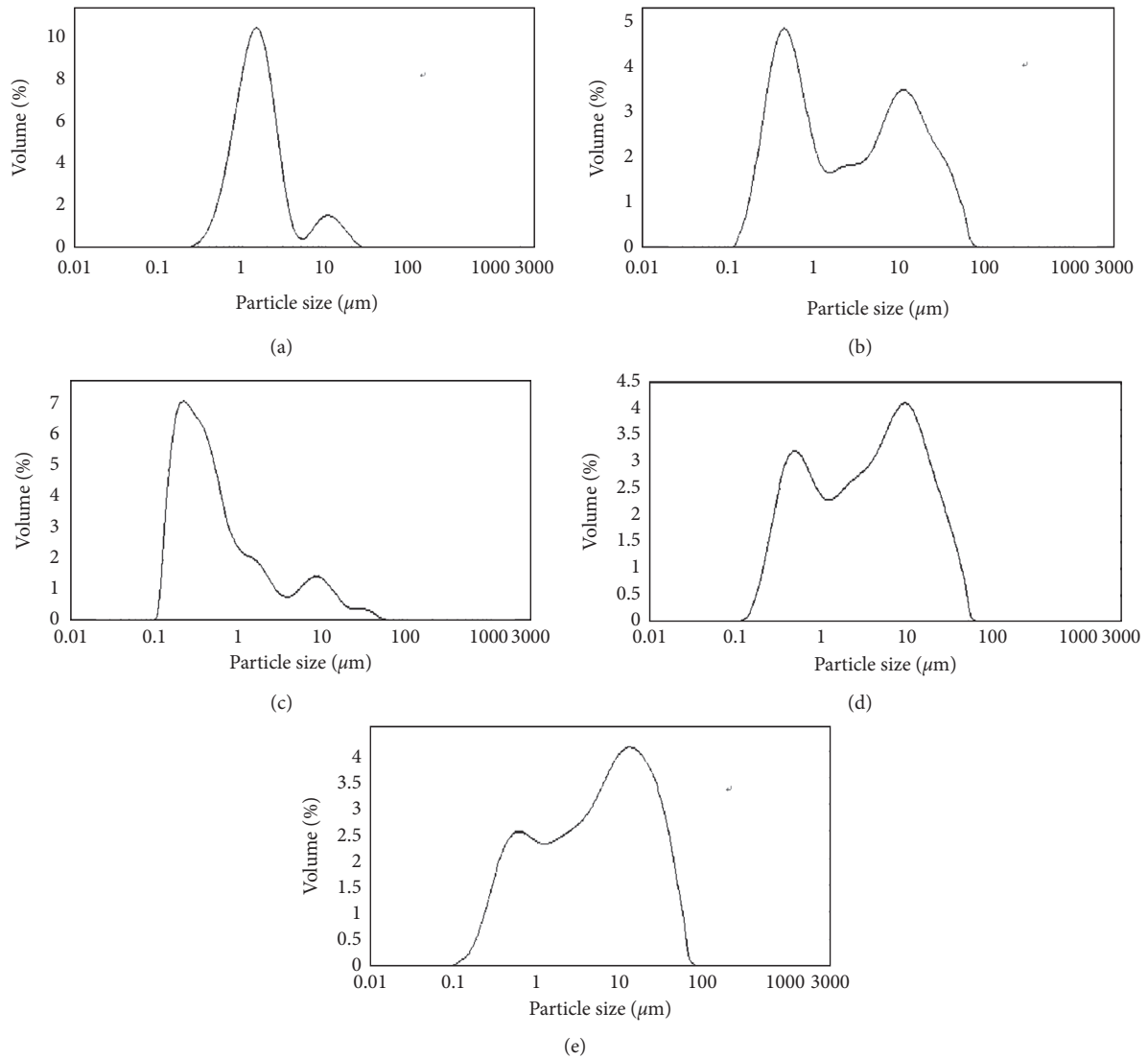


FIGURE 1: Size of the milled powder particles. (a) Milling 0 h. (b) Milling 0.5 h. (c) Milling 2 h. (d) Milling 5 h. (e) Milling 10 h.

volume fraction of NiO increases as a function of the milling time while that of  $\text{Fe}_2\text{O}_3$  shows an opposite trend. According to the X-ray diffraction pattern as shown in Figure 3, the calculated lattice constant of NiO and  $\text{Fe}_2\text{O}_3$  in the milled powders are given in Table 2. It can be seen that the lattice parameter of NiO increases from  $a = 4.1723 \text{ \AA}$  in the as-received powder to  $a = 4.1730 \text{ \AA}$  in the powder mixture milled for 5 h. This result reveals that some  $\text{Fe}_2\text{O}_3$  was dissolved into the lattice of NiO, which led to a decrease in the content of  $\text{Fe}_2\text{O}_3$  and a relative increase in that of NiO in the X-ray diffraction pattern. The lattice constants “a” and “c” of  $\text{Fe}_2\text{O}_3$  change frequently with the milling time, indicating the presence of the lattice distortion in the powder.

To investigate the interaction of the different powders in the milling process, SEM and EDX analysis of the typical milled powder mixture were performed. EDX analysis was done at least 10 points on each of the samples. The typical results are given in Figure 6. Here, independent  $\text{Fe}_2\text{O}_3$

particles were detected in the mixtures milled for no longer than 2 h (seen in Figures 6(a) and 6(b)). When the milling time increased to more than 2 h, no independent  $\text{Fe}_2\text{O}_3$  particles can be observed in the mixture powder (seen in Figures 6(c) and 6(d)). Moreover, Fe and Ni coexisted in the same powder particles but the content of Fe gradually decreased with increasing the milling time when the milling time was no less than 5 h, which implied that  $\text{Fe}_2\text{O}_3$  was dissolved into NiO in the further milling process. Figure 7 shows the microstrain  $\epsilon$  in the powders plotted against the ball-milling time. Since the elastic moduli  $E$  of  $\text{Fe}_2\text{O}_3$  and NiO were 201 and 126 GPa [18, 19], respectively, the third residual stress  $\sigma$  can be calculated according to Hooke’s law by utilizing the equation  $\sigma = E\epsilon$ . The third residual stresses obtained in the ball-milling process are shown in Figure 8.

The strain energy of the milled powders could be calculated according to equation  $W = (1/2) E\epsilon^2$  [20], and the relevant results can be calculated using the data in Figure 7,

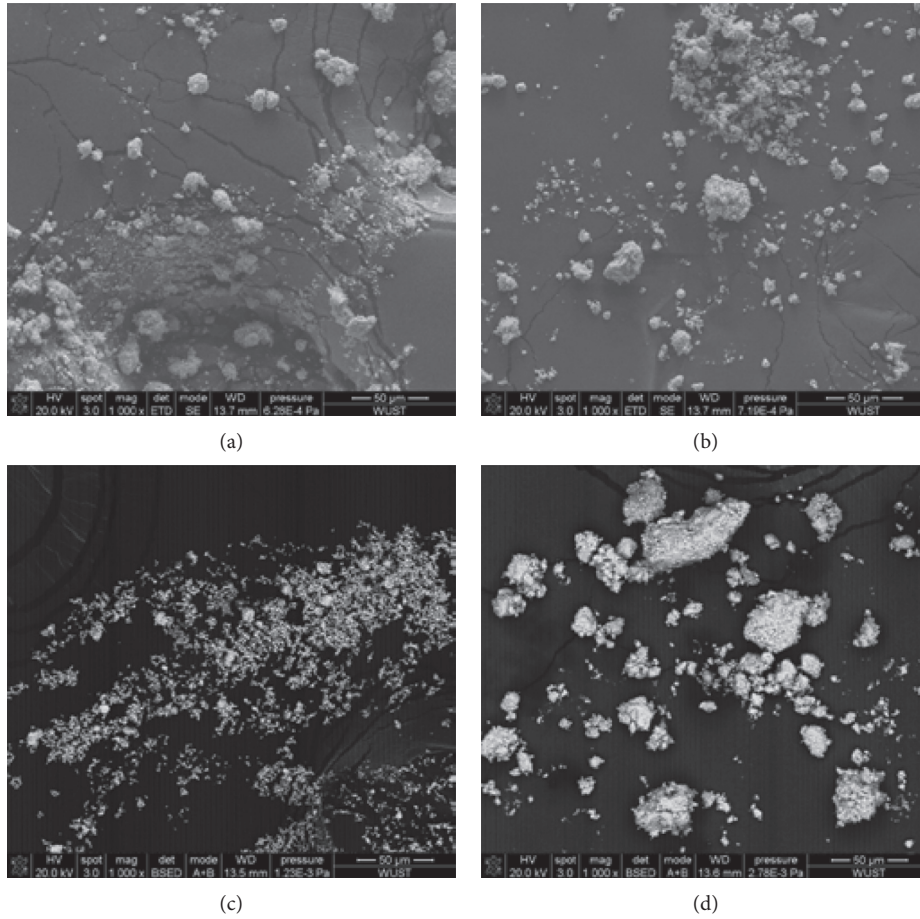


FIGURE 2: Secondary electron images (SEI) in SEM of the milled powders with different milling time; (a) for 0 h, (b) for 0.5 h, (c) for 2 h, (d) for 10 h.

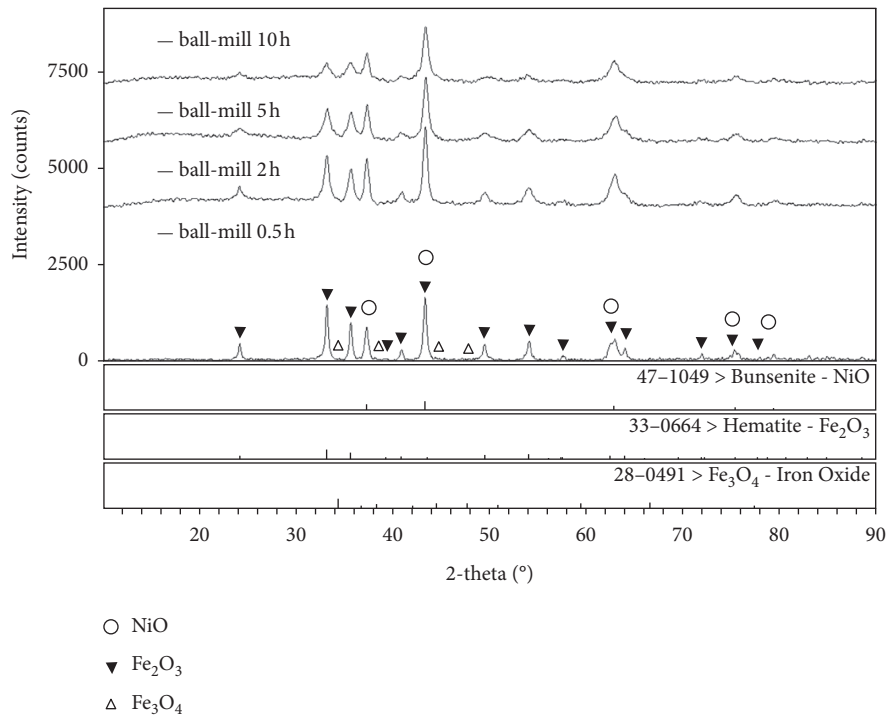


FIGURE 3: XRD diffraction patterns of the ball-milled powders with different milling time.

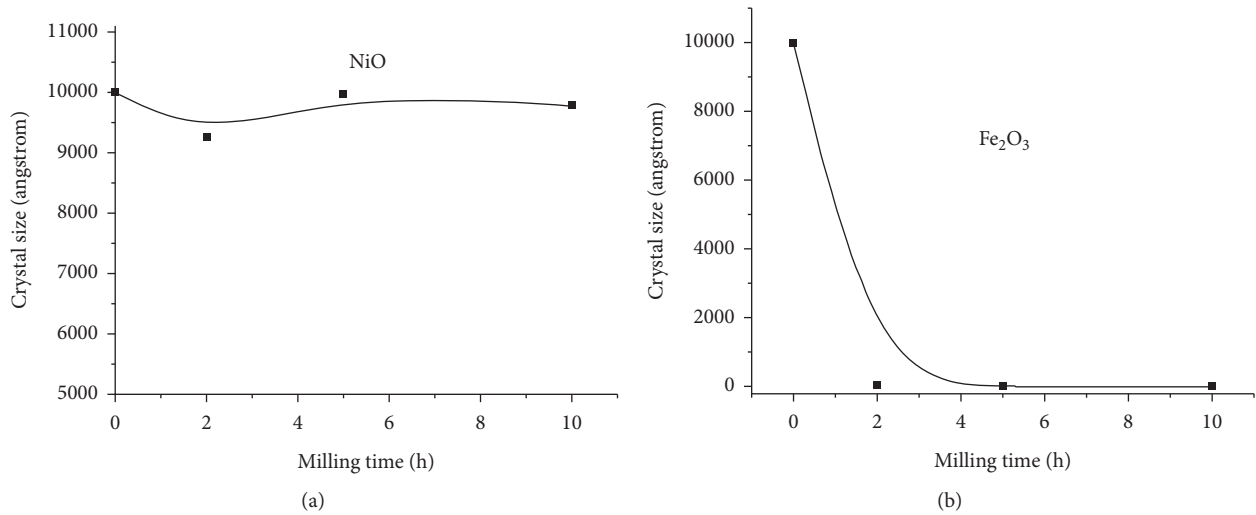


FIGURE 4: The effect of ball-milling on the grain size; (a) NiO. (b) Fe<sub>2</sub>O<sub>3</sub>.

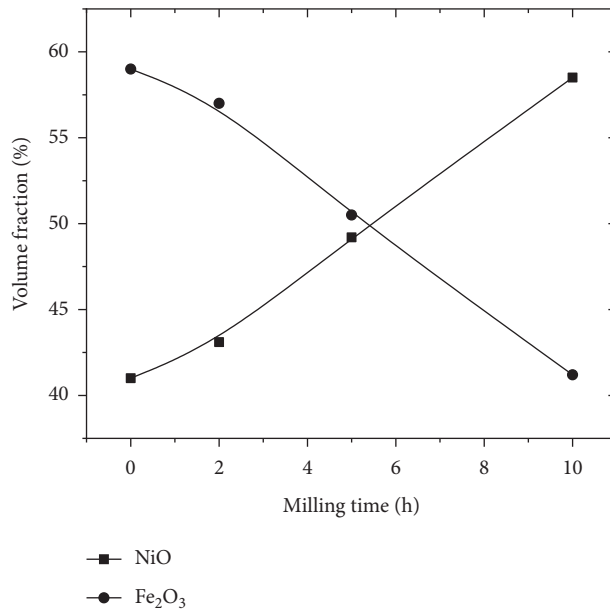


FIGURE 5: The measured volume fraction plotted against the ball-milling time.

TABLE 2: The average lattice constant of NiO in the milled powders/(Å).

		0h	0.5 h	2 h	5 h	10 h
Lattice constant	a	4.1723	4.1721	4.1724	4.1730	4.1725
	b	5.0342	5.02773	5.02656	5.03301	5.03177
	c	13.746	13.74831	13.75972	13.7505	13.7762

as shown in Figure 9. The strain energy of the milled powders initially increased with increasing the milling time, which peaked at a certain point and then decreased thereafter.

The microstructure evolution in the mixing process would possibly affect the synthesis reaction of the mixed Fe<sub>2</sub>O<sub>3</sub> and NiO in the following sintering process. Before the sintering experiment, the sintering temperature was determined by DSC (see Figure 10). A maximum temperature of

1450°C was used in the DSC measurement. Figure 10 demonstrates that the shapes of the DSC curves of the powders milled for 0, 2, and 10 h at temperatures below 1200°C are similar. However, an exothermic peak could be observed in the powders without milling at 1340°C (seen in Figure 10(a)), which may correspond to the transformation point of the mixture powder into NiFe<sub>2</sub>O<sub>4</sub>. In DSC curve of the milled powders, an obvious endothermic peak could be

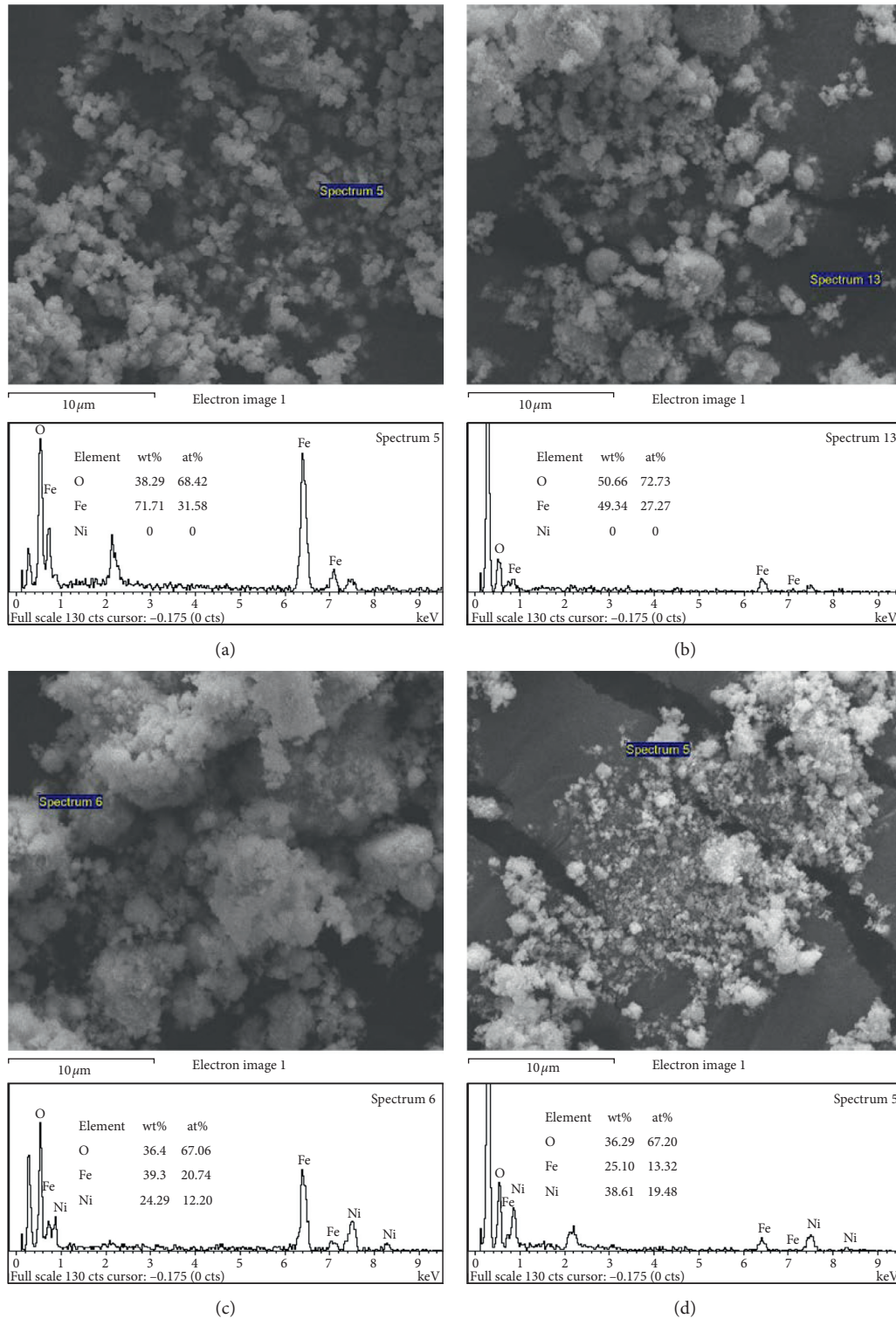


FIGURE 6: SEI in SEM together with typical EDS spectra of the milled powders with different milling time; (a) for 0 h (b) for 2 h (c) for 5 h (d) for 10 h.

observed after milling for 2 h (Figure 10(b)) and 10 h (Figure 10(c)) at about 1340°C, as well. Thus, 1340°C was used as the temperature for sintering.

Figure 11 shows the XRD patterns of the sintered powders which were ball-milled for 0, 2, 5, and 10 h, respectively. Good agreement in terms of the diffraction angles

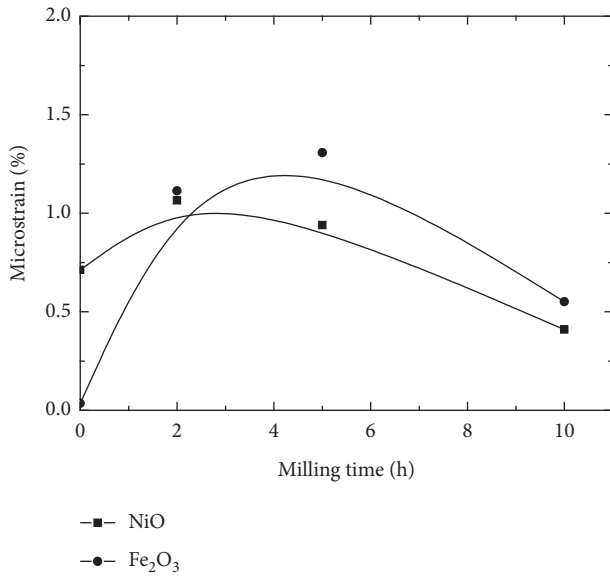


FIGURE 7: Measured micro-strain in the milled powders.

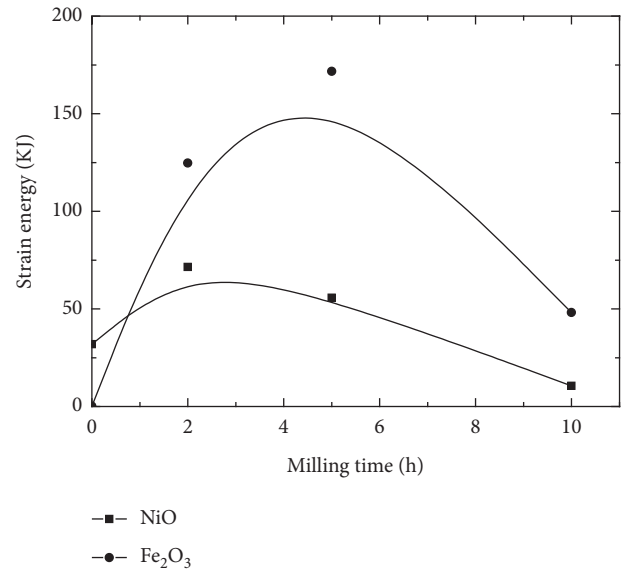


FIGURE 9: Strain energy in the milled powders.

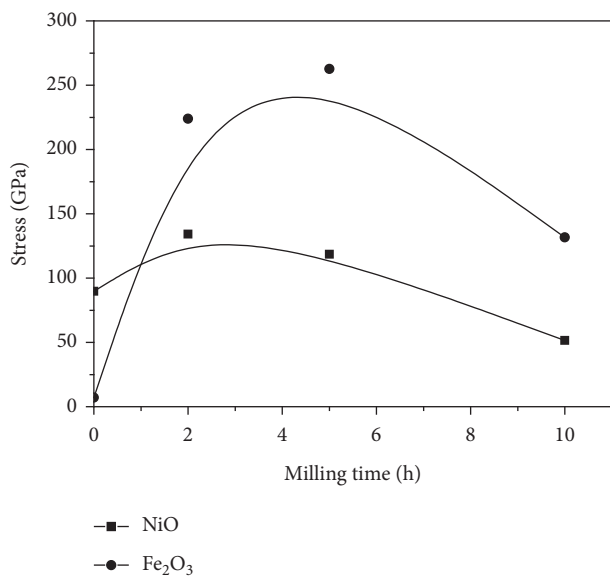


FIGURE 8: The micro-residual stress in the milled powders.

and the intensities could be observed between the pattern of the sintered powder without the ball-milling and the standard pattern of NiO (PDF File no.10-325).

#### 4. Discussions

The high-energy ball-milled powder particle sizes illustrated in Figure 1 show that these sizes were changed during the ball-milling. Primarily, the small particles tended to attach to the large particles, which enhanced the volume fraction of the large ones. A further ball-milling, for instance, the ball-milling for 2 h, caused decreases in the size of both the coarse and the fine powder particles, which indicated that the particles were broken. After a ball-milling for over 2 h, e.g., 5 h and 10 h, the volume fraction of the coarse particles

increased while that of the fine powders decreased. The activity of the powder particles at this stage can be an agglomeration of the fine powder particles and partially attached to the coarse particles, resulting in increasing the volume fraction of the coarse powder particles.

Those illustrated in Figure 2 are the SEM images of the mixed powders obtained at different milling times, which shows that the sizes of the powder particles vary with the milling time. It seems that the size changes of the powder particles with the milling time may be divided into three stages. At the primary milling stages, the powder particle size increased with increasing the milling time (seen in Figures 2(a) and 2(b)). And then the size decreased with an increase in the milling time (seen in Figures 2(b) and 2(c)) at a further milling stage. In the third stage, the powder particle size increased with increasing the milling time again (seen in Figures 2(c) and 2(d)). These three stages implied different physical behavior of the powder particles in the milling process. At the primary milling stage, the small Fe<sub>2</sub>O<sub>3</sub> powder particles were easier to be broken than the large NiO powder particles. The smaller broken pieces of Fe<sub>2</sub>O<sub>3</sub> tended to attach to the larger NiO particles, resulting in increases in both the volume fraction and the average size of the milled NiO particles. This finding also indicates that NiO is more difficult to break than Fe<sub>2</sub>O<sub>3</sub> (Figure 1). In the second stage of ball-milling, the broken Fe<sub>2</sub>O<sub>3</sub> powder particles became too small to deform further and to separate the adjacent NiO powder particles from each other. Thus, more opportunities for the collisions among NiO particles occurred, which resulted in the breakage of the NiO particles. It is noted that the average size of the NiO powder particles decreased at this stage. Finally, the average particle sizes of both NiO and Fe<sub>2</sub>O<sub>3</sub> increased once more because the temperature rising in the mixture powders were brought about by the collisions between different adjacent powder particles, and between powder particles and the wall of the jar mill. These temperature increments enhanced the adhesive property of all

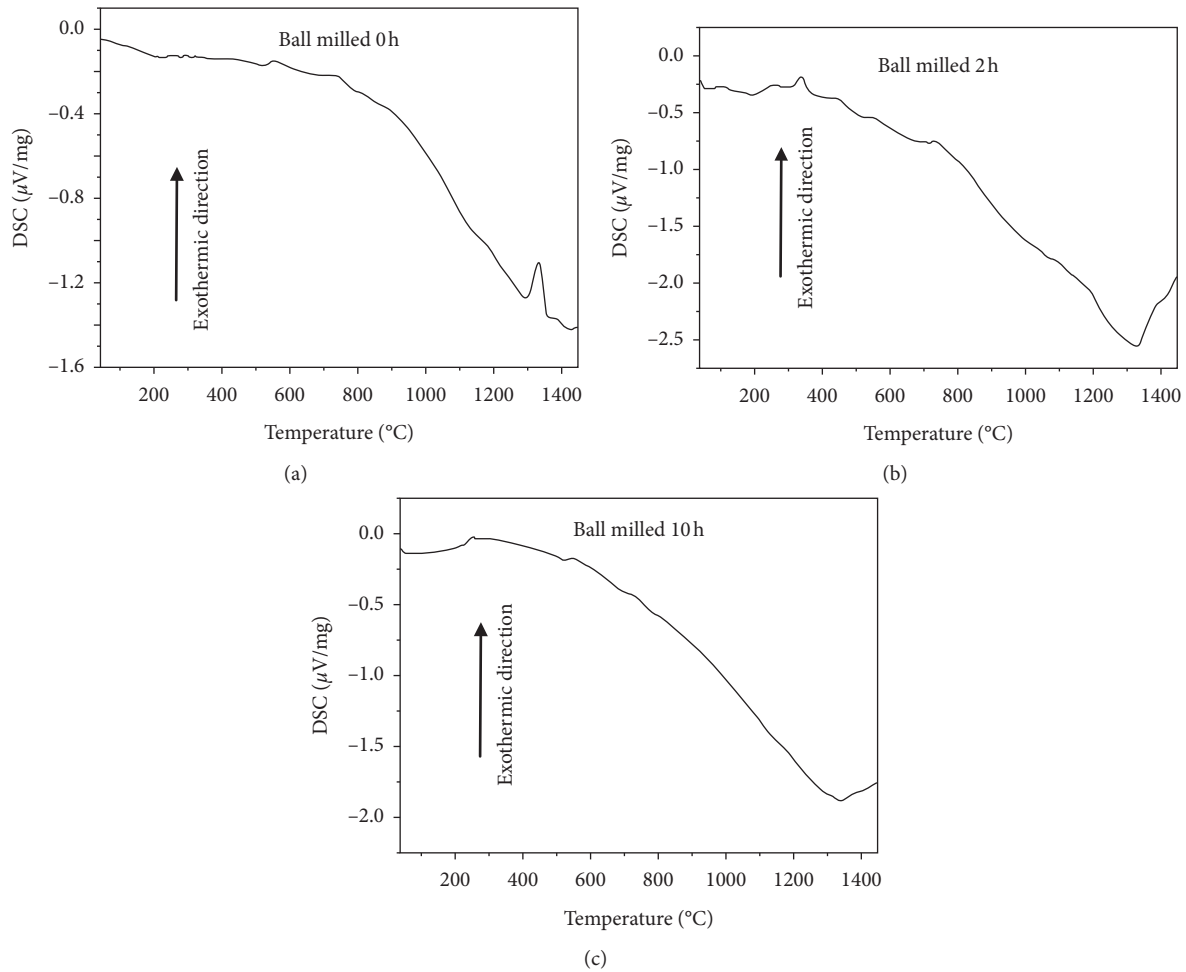


FIGURE 10: DSC curve of the milled powders with different milling time; (a) for 0 h; (b) for 2 h; (c) for 10 h.

the powders, thereby leading to the aggregation of these powder particles, and further increased the average size of the milled particles.

The strain energy of Fe<sub>2</sub>O<sub>3</sub>, as shown in Figure 9, changes more dramatically than that of NiO, which implies that the plastic deformation is more susceptible to occurring in Fe<sub>2</sub>O<sub>3</sub> than that in NiO in the ball-milling process. The deformation process can be clarified as follows: in the primary milling stage, the main physical processes occurring in the powders were the breakage of particles and the accumulation of strain in the powders. High-speed collisions between the adjacent powder particles, between the powder particles and the milling balls, and between the powder particles and the container wall generated a large amount of heat, which enhanced the temperature of the powders [21]. In this milling stage, the temperature in the powders was not high enough to lead to the recovery of them. If the milling time was adequately long, the temperature would increase to that higher than the recovery temperature of the powders. Thus, the strain energy in the powders tended to decrease. When these decreases in the strain energy were balanced by the increases in the strain energy caused by the powder deformation, the total strain energy reached a peak. After this peak, the temperature of the powders, for instance, in

Fe<sub>2</sub>O<sub>3</sub> milled for 5 h, was high enough to “soften” the powders. Therefore, strain energy decreased with increasing milling time.

As shown in Figure 10, the shift from an exothermic process to an endothermic one caused by the ball-milling may be due to the changes in the reaction products, the changes in the reaction pathways, or both.

According to the XRD results shown in Figures 3 and 11, the ball-milling leads to a solid solution of Fe<sub>2</sub>O<sub>3</sub> into the lattice of NiO, which expands the lattice constant of the latter (see Table 2). It is also reported that the strong internal strains introduced during mechanical milling treatment causes change in lattice constant and results in the unit cell expansion [22, 23]. The solid solution of the ferrite ion into the FCC NiO interstice and the severe distortion in the NiO lattice caused by the high-energy milling would probably result in a rearrangement of ferrite ion in the NiO lattice in the following sintering process. Thus, an obvious increasing in the intensity of the (311) face in the formed NiFe<sub>2</sub>O<sub>4</sub> X-ray diffraction pattern can be seen with increasing the milling time (see Figure 11). This rearrangement of the ferrite ion in the sintering process would absorb additional energy which finally affected the DSC curve of the milled powders (see Figure 10).

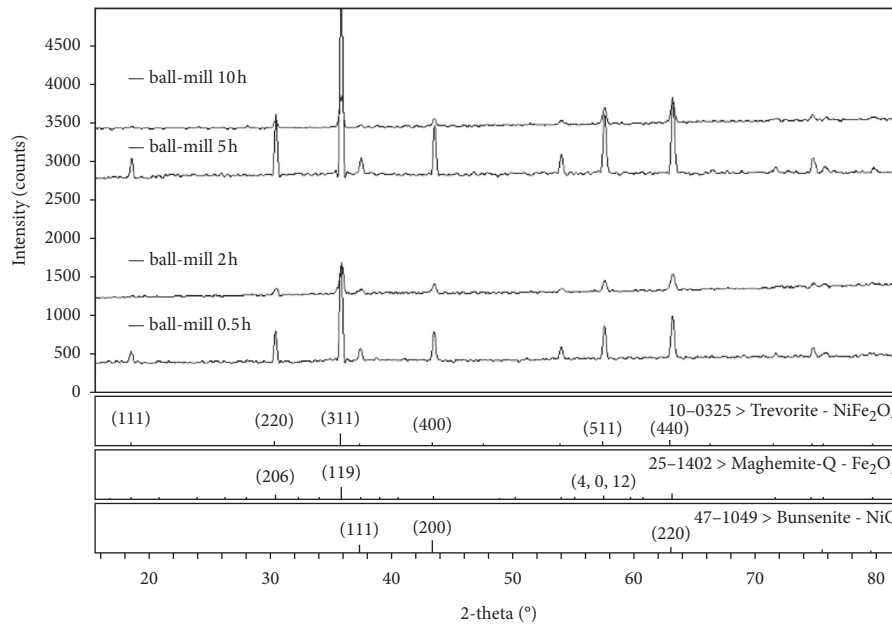


FIGURE 11: XRD diffraction pattern of the milled powders after sintered 1340°C for 0.5 h.

## 5. Conclusions

- (1) Powder particle size decreases with increasing the milling time up to 2 h, while powder particle size increases with increasing the milling time when the time is longer than 2 h.
- (2)  $\text{Fe}_2\text{O}_3$  powder particles are extensively broken and deformed during the ball-milling, whereas the size of NiO powder particles changes very slightly.
- (3) The ball-milling leads to a solid solution of iron atoms into the lattice of NiO, which delays the reaction of the powders during the following sintering process.

## Data Availability

The data in the article are available if necessary.

## Conflicts of Interest

The authors declare that they have no conflicts of interest.

## Acknowledgments

The authors appreciate the supports from the National Key R&D Program of China (no. 2017YFE0117400) and the National Natural Science Foundation of China (no. 51675007).

## References

- [1] J. Akter, K. P. Sapkota, and H. M. Abu, "Kinetically controlled selective synthesis of  $\text{Cu}_2\text{O}$  and  $\text{CuO}$  nanoparticles toward enhanced degradation of methylene blue using ultraviolet and sun light," *Materials Science in Semiconductor Processing*, vol. 123, Article ID 105570, 2021.
- [2] J.-R. Yang, Y. Wang, and H. Chen, "A new approach for the effective removal of  $\text{NO}_x$  from flue gas by using an integrated system of oxidation absorption biological reduction," *Journal of Hazardous Materials*, vol. 404, Article ID 124109, 2021.
- [3] J. Liu, H. Wang, R. Ye, P. Jian, and L. Wang, "Promotional effect of Mn-doping on the catalytic performance of NiO sheets for the selective oxidation of styrene," *Journal of Colloid and Interface Science*, vol. 585, pp. 61–71, 2021.
- [4] A. Nadar, A. Banerjee, and M. R. Pai, "Immobilization of crystalline  $\text{Fe}_2\text{O}_3$  nanoparticles over  $\text{SiO}_2$  for creating an active and stable catalyst: a demand for high temperature sulfuric acid decomposition," *Applied Catalysis B-Environmental*, vol. 283, Article ID 119610, 2021.
- [5] S.-T. Harrison, T. Garcia, K. Edilma, B. Meneses, and C. Augusto, "Cation vacancies in  $\text{NiFe}_2\text{O}_4$  during heat treatments at high temperatures: structural, morphological and magnetic characterization," *Materials Research-Ibero-American Journal of Materials*, vol. 22, no. 5, 2019.
- [6] A. Kumar, P. Dhekne, and A. K. Swarnakar, "Phase evolution of  $\text{CoCrCuFeNiSix}$  high-entropy alloys prepared by mechanical alloying and spark plasma sintering," *Materials Research Express*, vol. 6, no. 2, 2019.
- [7] F. Deirmina and M. Pellizzari, "Strengthening mechanisms in an ultrafine grained powder metallurgical hot work tool steel produced by high energy mechanical milling and spark plasma sintering," *Materials Science and Engineering: A*, vol. 743, pp. 349–360, 2019.
- [8] Y. Shi, J. Ding, X. Liu, and J. Wang, " $\text{NiFe}_2\text{O}_4$  ultrafine particles prepared by co-precipitation/mechanical alloying," *Journal of Magnetism and Magnetic Materials*, vol. 205, no. 2–3, pp. 249–254, 1999.
- [9] Y. S. Cho and C. C. Coch, "Structural evolution in  $\text{Nb}_3\text{Sn}$  during mechanical attrition," *Materials Science and Engineering: A*, vol. 141, no. 1, pp. 139–148, 1991.
- [10] A. K. Bhattacharya and E. Arzt, "Diffusive reaction during mechanical alloying of intermetallics," *Scripta Metallurgica et Materialia*, vol. 27, no. 5, pp. 635–639, 1992.

- [11] D. R. Maurice and T. H. Courtney, "The physics of mechanical alloying: a first report," *Metallurgical Transactions A*, vol. 21, no. 1, pp. 289–303, 1990.
- [12] M. Konarova and I. Taniguchi, "Preparation of carbon coated LiFePO<sub>4</sub> by a combination of spray pyrolysis with planetary ball-milling followed by heat treatment and their electrochemical properties," *Powder Technology*, vol. 191, no. 1-2, pp. 111–116, 2009.
- [13] Y. Z. Zhu and Z. M. Yin, "Pressing vacuum sintering of multipowders for manufacturing novel engine valve seat on Gleeble 1500 simulator," *Powder Metallurgy*, vol. 52, pp. 41–48, 2009.
- [14] C. Santos, M. H. Koizumi, J. K. M. F. Daguano, F. A. Santos, C. N. Elias, and A. S. Ramos, "Properties of Y-TZP/Al<sub>2</sub>O<sub>3</sub> ceramic nanocomposites obtained by high-energy ball milling," *Materials Science and Engineering: A*, vol. 502, no. 1-2, pp. 6–12, 2009.
- [15] Y. Z. Zhu, Z. M. Yin, Z. D. Xiang, and Z. Zhe, "Cold densification behaviour of multiple alloy powder containing Fe-Cr and Fe-Mo hard particles," *Powder Metallurgy*, vol. 51, no. 2, pp. 143–149, 2008.
- [16] H.-B. He, "Effect of Yb<sub>2</sub>O<sub>3</sub> doping on the grain boundary of NiFe<sub>2</sub>O<sub>4</sub>-10NiO-based cermets after sintering," *International Journal of Minerals, Metallurgy, and Materials*, vol. 22, no. 12, pp. 1334–1341, 2015.
- [17] J. Du, Y. Liu, G. Yao, X. Long, G. Zu, and J. Ma, "Influence of MnO<sub>2</sub> on the sintering behavior and magnetic properties of NiFe<sub>2</sub>O<sub>4</sub> ferrite ceramics," *Journal of Alloys and Compounds*, vol. 510, no. 1, pp. 87–91, 2012.
- [18] K. TANAKA, Y. Doi, Y. Akiniwa, H. Sumi, Y. Mizutani, and K. Ukai, "Elastic constants for X-ray stress measurement of ceramics for solid oxide fuel cell (SOFC)," *Journal of the Society of Materials Science, Japan*, vol. 54, no. 10, pp. 1080–1086, 2005.
- [19] R. W. Makkay, G. H. Geiger, and M. E. Fine, "Elasticity and internal friction of  $\alpha$ -Fe<sub>2</sub>O<sub>3</sub>," *Journal of Applied Physics*, vol. 33, no. 3, pp. 914–916, 1962.
- [20] P. Van Pham, "Solutions of the interfacial shear and normal stresses in plate flexural-strengthened beams based on different complementary strain energy assumptions," *Engineering Structures*, vol. 229, Article ID 111567, 2021.
- [21] I. Tomohiro, K. Kazunori, and Y. Tomoya, "Novel mechanochemical process for synthesis of magnetite nanoparticles using coprecipitation method," *Advanced Powder Technology*, vol. 20, no. 6, pp. 521–528, 2009.
- [22] A. R. Tanna and H. H. Joshi, "Influence of mechanical milling on structural and magnetic properties of Cu<sup>2+</sup> substituted MnFe<sub>2</sub>O<sub>4</sub>," *Indian Journal of Physics*, vol. 90, no. 9, pp. 981–989, 2016.
- [23] A. R. Tanna, S. S. Srinivasan, and H. Joshi, "Enhancement in magnetoelectric properties of lead-free multiferroic composite through high-energy mechanical milling," *Journal of Materials Science: Materials in Electronics*, vol. 31, no. 12, pp. 9306–9320, 2020.